

Zeolite Crystal Growth

Unraveling the Twin and Tunability of the Crystal Domain Sizes in the Medium-Pore Zeolite ZSM-57 by Electron Crystallography

Lei Wang,^{+, [a]} Nana Yan,^{+, [a, b]} Xiaona Liu,^[a, b] Xuebin Zhao,^[a, b] Meikun Shen,^[c] Leifeng Liu,^[d] Peng Tian,^[a] Peng Guo,^{*, [a]} and Zhongmin Liu^{*, [a]}

Abstract: Tailoring the morphology of a specific crystalline material through distinct crystal growth mechanisms (classical and nonclassical) is challenging. Herein, we report the two unique morphologies of a medium-pore (10×8-ring) zeolite, ZSM-57, prepared by employing an identical organic structure-directing agent (OSDA) and different inorganic cations, namely Na⁺ and K⁺, denoted as ZSM-57-Na (pentagonal nanoplates) and ZSM-57-K (pentagonal nanoprisms), respectively. The tunable twin domain size and twin boundaries in both samples have been unraveled at the atomic level by electron crystallography. It is of significance to note that the 10-ring pore openings run perpendicular to the pentagonal nanoplates and nanoprisms. Moreover, the dis-

tinct crystal growth mechanisms, which result in the different unique morphologies and tunable twin domains, were further determined by electron crystallography combined with other techniques. Nonclassical growth involving the aggregation of amorphous aluminosilicate nanoparticles to the smooth ZSM-57-Na crystal surface dominates the ZSM-57-Na crystallization process. For the ZSM-57-K sample, the classical layer-by-layer growth through the addition of silica molecules to advancing steps on the crystal surface dominates the ZSM-57-K crystallization process. The different morphologies of both samples result in the distinct catalytic lifespan of the methanol conversion and selectivity of lower olefins.

Introduction

Conventional zeolites are crystalline microporous aluminosilicates possessing well-defined cavities or channels of molecular size. The basic building unit, the TO₄ (T = Si or Al) tetrahedron, is further connected through corner-sharing to generate a three-dimensional (3D) zeolite framework. Until now, there have been 239 framework type codes (FTCs) approved by the International Zeolite Association-Structure Committee (IZA-SC).^[1] According to the pore window delimited by the number of TO₄ tetrahedra, zeolites can be categorized into small pore (by 8 TO₄), medium pore (10 TO₄), large pore (12 TO₄), and

extra-large pore (≥ 12 TO₄) zeolites. On one hand, many endeavors have been devoted to synthesizing new zeolites with fascinating topologies, thereby enriching zeolite structural diversity. On the other hand, tailoring the morphologies of known zeolites for desirable catalytic properties by tuning twin domains, stacking disorders, and rotational or epitaxial intergrowth has received increasing attention in academic science and industry.^[2–4] Crystal twinning occurs when separated crystals with the same crystallographic structure join by such symmetry operations as the mirror plane, rotation axis, or inversion center. For instance, multi-twinning components with pyramidal boundaries in the ZSM-5 zeolite (FTC: MFI) have been uncovered by the electron backscatter diffraction (EBSD) method.^[5,6] In the stacking disorder phenomenon, identical building layers with different stacking manners along the third dimension are identified. This phenomenon, frequently observed in the *BEA, *-ITN, *MRE, *SSO, and *STO zeolite families, has been extensively investigated.^[7–14] Very recently, the overlap of an independent crystal twin and stacking disorder in the MTW-type zeolite along different dimensions derived an extremely complex fractal structure.^[2,15] Moreover, the rotational or epitaxial intergrowth of structurally related zeolites such as MFI/MEL and FAU/EMT will result in novel hierarchical zeolite architectures. For example, the MEL and EMT nanodomains embedded in the MFI and FAU nanoflakes induce the self-pillared zeolite sheet and house-of-cards nanosheet structures, respectively.^[16–18]

Probing these structural features at the atomic level will shed light on the mechanism of crystal growth and structure–


[a] L. Wang,⁺ N. Yan,⁺ X. Liu, X. Zhao, P. Tian, P. Guo, Z. Liu
National Engineering Laboratory for Methanol to Olefins
Dalian National Laboratory for Clean Energy
Dalian Institute of Chemical Physics, Chinese Academy of Sciences
Dalian 116023 (P. R. China)
E-mail: pguo@dicp.ac.cn
zml@dicp.ac.cn

[b] N. Yan,⁺ X. Liu, X. Zhao
University of the Chinese Academy of Sciences, Beijing 100049 (P. R. China)

[c] M. Shen
Department of Chemistry, Washington University in St. Louis
1 Brookings Drive, St. Louis, 63130, Missouri (USA)

[d] L. Liu
School of metallurgy and materials, University of Birmingham
B15 2TT, Birmingham (UK)

[*] These authors contributed equally to this work.

 Supporting information and the ORCID identification number(s) for the author(s) of this article can be found under:
<https://doi.org/10.1002/chem.201804269>.

activity relationships. For such structural characterizations, high-resolution transmission electron microscopy (HRTEM) has been recognized as a powerful tool for investigating the sample of interest in real space and conventional two-dimensional (2D) selected area electron diffraction (SAED) in reciprocal space. The complexity of the well-known zeolite beta (FTC: *BEA) has mainly been explored by electron crystallography (imaging in real space and diffraction in reciprocal space).^[7,8] Recently, there was a breakthrough in the electron diffraction (ED) methodology, called rotation electron diffraction (RED).^[19,20] Compared with conventional 2D SAED, this technique can collect 3D ED data in reciprocal space from the individual nanocrystal. The unit cell parameters, space group, and diffraction intensities can be obtained from the RED data, which could be used for further structure solution by employing the known phasing algorithms.^[21–29] Until now, there have been various novel structures solved based on RED data.^[9,12,30–36]

Besides determining novel structures through electron crystallography, TEM is also one of the effective approaches used to probe the mechanism of zeolite growth. During the crystallization of zeolites, two concerted pathways have been identified: 1) Soluble molecules accrete on the crystal surface (classical) and 2) amorphous nanoparticles attach to the crystal surface (nonclassical).^[37–42] Crystal growth by the classical layer-by-layer mechanism exhibits a well-defined crystal habit, whereas the nonclassical mechanism involving attachment and subsequent rearrangement of amorphous precursors leads to an irregular morphology with a lack of distinct facets and/or rough surface features composed of protrusions with sizes equivalent to the precursors.^[38,39] The imaging and diffraction obtained from TEM can be employed to check the particle size of distinct populations and the spatial distribution of regions of interest,^[40] discriminate the amorphous and crystalline regions,^[38] analyze the crystallographic orientation of crystals,^[40,41] etc. during the crystallization process. Therefore, crucial features of the two different pathways could be distinguished by TEM associated with other approaches. For instance, in 2009, Zhou and co-workers studied the crystal growth in the early stages of formation of the zeolite LTA by TEM and scanning electron microscopy (SEM). They concluded that the precursor molecules undergo polymerization followed by nucleation and subsequent crystal growth. In the above system, the aggregation of nanoparticles does not occur and monoclinic zeolite A is formed, which can be categorized under the classical mechanism.^[43] In 2015, Rimer and co-workers monitored the growth mechanism of the small-pore zeolite SSZ-13 (CHA) by using a synergistic combination of ex situ TEM, SEM, powder X-ray diffraction (PXRD), atomic force microscopy (AFM) etc., and confirmed that the growth of SSZ-13 is dominated by particle attachment (the nonclassical mechanism) along with the addition of molecules (the classical mechanism).^[38] Up to now, tailoring the classical/nonclassical route in a heterogeneous system of a specific zeolite is still challenging.

In this work we not only unraveled tunable twin domains in the medium-pore (10×8-ring) zeolite ZSM-57 (FTC: MFS) by electron crystallography, including HRTEM, SAED, and the now-

developed RED technique, but also explored the distinct growth mechanisms of the ZSM-57 zeolite resulting in the different unique morphologies.

Results and Discussion

Structural characterizations of twin domains in ZSM-57-Na

ZSM-57 was initially synthesized by using *N,N,N,N',N',N'*-hexaethylpentanediammonium (abbreviated as Et₆-diquat-5) and Na⁺ as structure-directing agents (SDAs; denoted as ZSM-57-Na).^[45,46] It possesses 10-ring (5.4 Å×5.1 Å) and 8-ring (4.8 Å×3.3 Å) channels along the *a* and *b* axes, respectively, thereby generating a 2D channel system. Profile fitting of the PXRD pattern (see Figure S1 in the Supporting Information) verified that the as-prepared sample possesses the MFS topology after conventional hydrothermal synthesis at 433 K for 144 h. Its unit cell composition deduced from thermogravimetric (TG) and X-ray fluorescence (XRF) spectroscopy measurements is |(Et₆-diquat-5)_{0.76}Na_{0.44}(H₂O)_{0.99}(OH⁻)_{0.28}| [Si_{34.32}Al_{1.68}O₇₂] (see Table S1). The SEM images of the acquired samples, an example of which is exhibited in Figure 1a, show that the high-silica ZSM-57 (Si/Al=20.40) zeolite has a rare pentagonal nanoflake morphology (ca. 1 μm). The SEM images reflect that the pentagonal nanoflakes are composed of nanosized arrowhead-shape domains (NASDs). Although a similar morphology of this zeolite has been reported,^[46,47] the atomic structure and the origin of the pentagonal intergrowth manner remain elusive. From the low-magnification TEM image (Figure 1b), the pentagonal nanoflake is observed and made up of NASDs (20–50 nm, indicated by arrow), which is consistent with the SEM observations. The sharp dots of the SAED patterns collected from the pentagonal corner (Figure 1c) and edge (Figure 1d) indicate the nature of the single-crystal-like zeolite. It is of interest to note that both SAED patterns can be indexed by three electron diffraction (ED) datasets of ZSM-57 along the [100] axis (indicated by rectangular frames), which indicates the 10-ring channel system runs perpendicular to the pentagonal nanoflake. The presence of three ED datasets in Figure 1c,d indicates the aggregated NASDs at the edge or corner can be categorized into three specific crystallographic orientations. The evolution of both unique SAED patterns could be understood in the following way: Apart from the central set of the SAED pattern, another two SAED patterns overlap with the central one with rotation angles of about 74.2 and -74.2°, respectively (see Figure S2). In this case, the reflections 0*kk* (such as 011, 022, etc.) and 0-*kk* are shared among these three datasets (see Figure S2c), respectively. To simplify the explanation, the term “{0*kk*} crystallographic facet” replaced by “(011) crystallographic facet” will be used for the following illustration. The ED analysis indicates the (011) crystallographic plane will be the twin plane in real space. Analysis of the HRTEM images and their fast Fourier transformations (FFT) (Figure 1e,f and Figure S3) confirms the structural elucidation mentioned above. The intact NASD was segregated into smaller triangle domains (ca. 20 nm) shared by twin planes (indicated by straight white lines in Figure 1e,f). Furthermore, exposed exte-

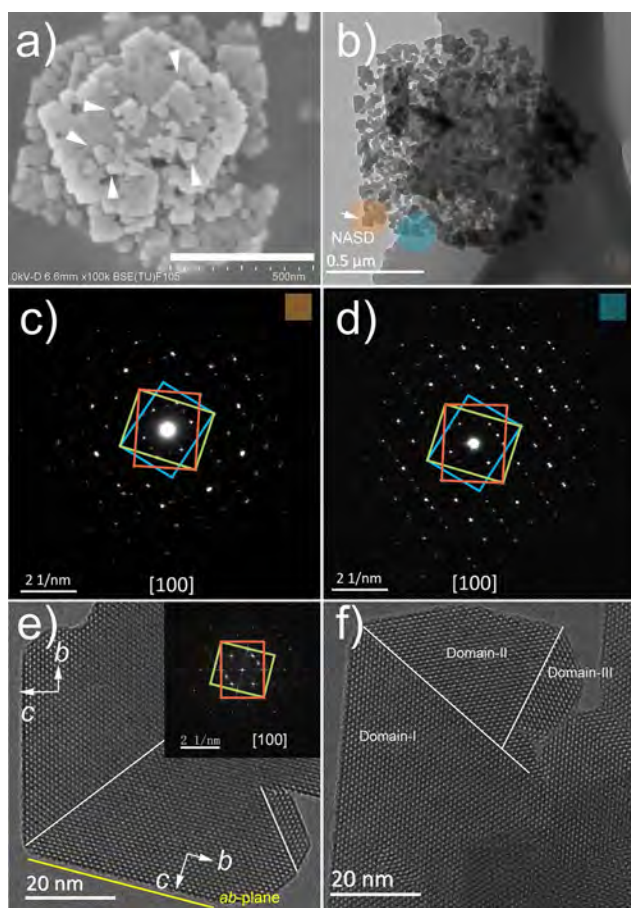


Figure 1. a) SEM image of the ZSM-57-Na zeolite and b) low-magnification TEM image of a single nanoflake of ZSM-57-Na. NASD is marked by the arrow. c,d) SAED patterns taken of the highlighted areas in Figure 1 b, respectively. HRTEM images of e) the composed NASD (highlighted orange area) and f) isolated fragment from the same sample. Straight white lines on the NASDs refer to the twin boundary, and the yellow line highlights the exposed exterior facets, deduced as *ab* planes.

rior facets of triangle domains are *ab* planes highlighted by the yellow straight line in Figure 1 e.

In the last paragraph, the structural features along the *a* axis (within the *bc* plane) have been elucidated. However, structural information along the *b* or *c* axis is challenging to obtain due to the preferred plate-like morphology. In this case, the newly-developed RED technique was applied to this sample to collect 3D ED data in reciprocal space. The reconstructed 3D reciprocal lattice demonstrates that there are no diffuse streaks along any direction, which indicates the absence of stacking disorder (see Figure S4a in the Supporting Information). It also manifests that all the NASDs share the *a* axis exactly without any tilting. This RED data can be further indexed by three ED datasets. An orthorhombic unit cell of ZSM-57 ($a=7.54 \text{ \AA}$, $b=14.39 \text{ \AA}$, and $c=19.02 \text{ \AA}$) could be deduced from one of the datasets. The 2D slice $0kl$ cut from the reconstructed reciprocal lattice confirms the presence of three ED datasets as well (see Figure S4b). According to the twin features in the ZSM-57-Na sample unraveled by electron crystallography, a plausible structure model can be built (Figure 2). The presence of twin do-

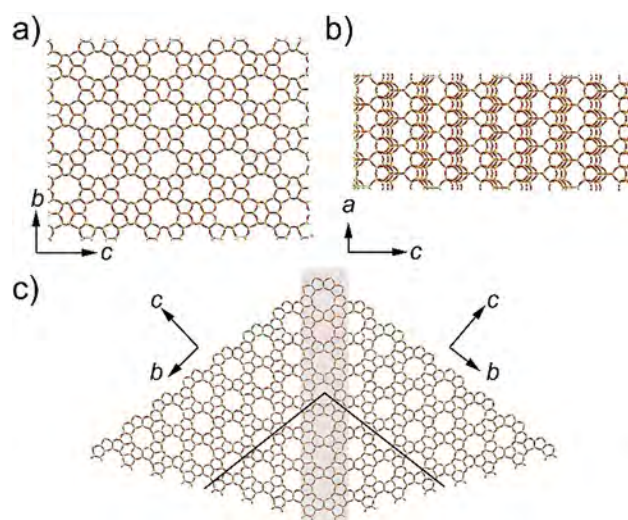


Figure 2. Framework of zeolite ZSM-57: a) 10-ring channels and b) 8-ring channels running straight along the *a* and *b* axes, respectively. c) Atomistic structure model of two vicinal twin domains with a fixed twin angle of about 105.8° (highlighted area: twin boundary, outline: “V-shaped” 8-ring channels).

ains changes the straight 8-ring channel to a “V-shaped” structure in the *bc* plane of the MFS framework (Figure 2 c). In contrast to the intergrowth of zeolite X/A^[48] and the MTW-type zeolite,^[2] no novel second building units on the twin boundary in the MFS-type zeolite can be found.

Structural characterizations of twin domains in ZSM-57-K

A typical synthesis of ZSM-57 can be considered a synergy of the inorganic and organic SDAs. Inspired by the empirical synthetic strategy employed by the pioneers of the field to construct this hybrid system, it is of significance to point out that the inorganic cation plays a significant role in the phase selectivity^[30,49,50] and modification of the morphology^[51] when the OSDA is kept the same. For example, we have rationally designed and synthesized a zeolite family with expanding structural complexity and embedded isorecticular structures by employing the identical OSDA (tetraethylammonium, TEA⁺) and different inorganic cations.^[30] Furthermore, the introduction of inorganic cations into the zeolite synthetic system would entail a morphological change in the final products. For instance, in the synthesis of SUZ-4 (SZR), different Na⁺/K⁺ ratios in the synthetic system can alter the morphology from long fibers to nanorods.^[51] These pieces of inspiring work encouraged us to study the influence of inorganic cations in the synthesis of ZSM-57.

Pure ZSM-57 zeolites could be synthesized by replacing Na⁺ with K⁺ ions (see Figure S1 in the Supporting Information), denoted as ZSM-57-K. It is worth noting that the ZSM-57-K sample contains an intact crystal structure (ca. 300 nm) with a pentagonal geometry (Figure 3 a,b). In contrast to the NASDs observed in the ZSM-57-Na sample, much denser pentagonal nanoprisms with smooth surfaces are observed in ZSM-57-K. The SAED pattern of the edge (Figure 3 c) shows the single-

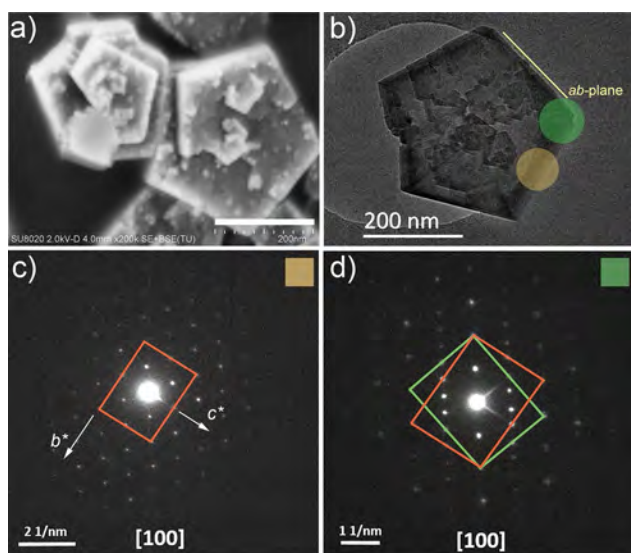


Figure 3. a) Typical SEM morphology and b) TEM image of the ZSM-57-K zeolite. c,d) SAED patterns of highlighted areas in Figure 3 b, respectively.

crystal nature of a larger triangle domain (ca. 150 nm) and can be indexed as the [100] zone axis. Figure 3 d illustrates that the SAED pattern of the corner of the pentagonal-shaped crystal can be interpreted by two ED datasets of ZSM-57 along the [100] direction but with a rotation angle of around 74.2° . They also share $0kk$ reflections, which implies that the twin plane is the (011) crystallographic plane. Exposed exterior facets of larger triangle domains can be deduced as the ab planes as well (yellow straight line in Figure 3 b). Larger triangle domains with a twin angle of around 74.2° cannot completely fill the circle angle, which results in the overlapped area between the initial and the final triangle domain. The RED data collected from an isolated pentagonal prism also demonstrates that all these larger triangle domains share the a axis without any tilting (see Figure S5). The above investigation demonstrates that the single domain size can be tuned from around 20 nm to around 150 nm by changing the inorganic cation.

Crystallization mechanism of ZSM-57-Na

The aggregation of NASDs detected in ZSM-57-Na and the smooth surface observed in ZSM-57-K indicate that distinct crystallization processes might occur in their formation. Thus, the evolution of the crystallization process was initially monitored by ex situ XRD, SEM, and TEM. It is of interest to point out that phase transitions occur in both systems (Figure 4) and the structural characterizations of the two intermediate phases (denoted as ZSM-57-Na-Inter and ZSM-57-K-Inter) are still under investigation.

For the ZSM-57-Na sample, the sol-gel obtained after stirring overnight consists of the silica and alumina sources and/or soluble aluminosilicate molecules as well as aggregated amorphous precursors (ca. 20 nm, as suggested by TEM analysis of the supernatant, see Figure S6a,b in the Supporting Information). The SEM image of the ZSM-57-Na sample after the

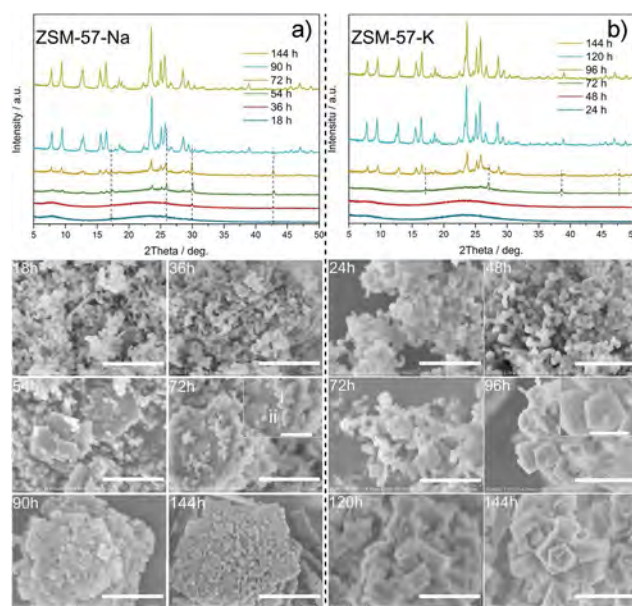


Figure 4. PXRD patterns (top) and SEM images (bottom) showing the evolution process of a) ZSM-57-Na and b) ZSM-57-K zeolites. The dashed lines in the PXRD patterns indicate the intermediate phases of each system. In the SEM images, the scale bar equates to 500 nm. Inset to ZSM-57-Na, 72 h: i: WLPs, ii: ZSM-57-Na plate, scale bar: 200 nm.

first 18 h of reaction shows homogeneous nanoparticles of the amorphous precursor (20–50 nm, Figure 4 a, 18 h). A small amount of ZSM-57-Na-Inter with a smooth surface and around 200 nm in size starts to appear (as verified by PXRD and SEM, Figure 4 a, 18 h) in this system. After 36 h of heating, the individual particles seem to merge and cross-link together to form amorphous worm-like particles (WLPs, Figure 4 a, 36 h and Figure S7), which have been recognized as typical precursors in the heterogeneous medium of zeolite synthesis, for example, **CHA**-,^[38] **MFI**-,^[52] **MTW**-,^[41] **TON**-,^[53] **LTL**-,^[42] and **GIS**-type^[54] zeolites. In the sample after 54 h of heating, initial pentagonal nanoplates with a smooth surface (ca. 400 nm) can be observed, which have been identified as ZSM-57-Na nanoplates by PXRD, HRTEM, and SAED (Figure 4 a, 54 h, and Figure 5). None of the nanosized crystalline domains can be observed in these initial pentagonal ZSM-57-Na nanoplates and only a few large single domains (ca. 200 nm) can be detected, the structural features of which resemble the final ZSM-57-K sample. Thus, in this 54 h period, three distinct phases coexist, namely a large amount of WLPs, a few ZSM-57-Na-Inter, and the initial pentagonal ZSM-57-Na nanoplates. Upon extending the reaction time to 72 h, an increasing amount of pentagonal ZSM-57-Na nanoplates form accompanied by numerous WLPs (Figure 4 a, 72 h, i) attached to their surfaces (Figure 4 a, 72 h, ii and Figure S8). Therefore, the formerly smooth surfaces and outer edges of the initial pentagonal ZSM-57-Na nanoplates become rough terrains. The ZSM-57-Na-Inter is still present at this stage, as demonstrated by the PXRD data in Figure 4 a. After heating for 90 h, the ZSM-57-Na-Inter phase is consumed completely (Figure 4 a, 90 h). As the reaction time increases, more and more amorphous WLPs attach to the pentagonal

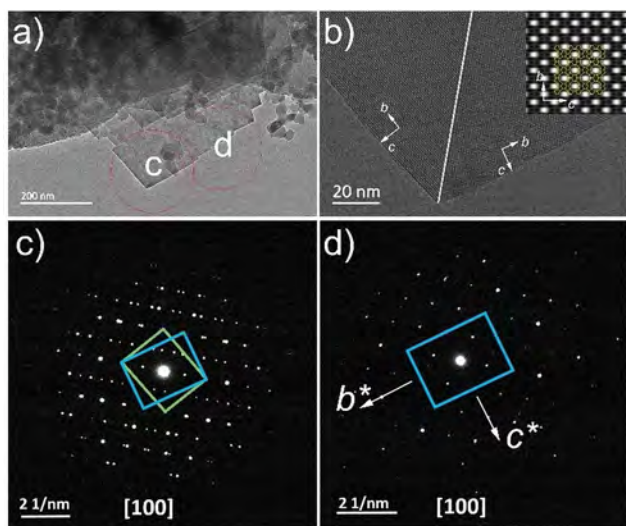
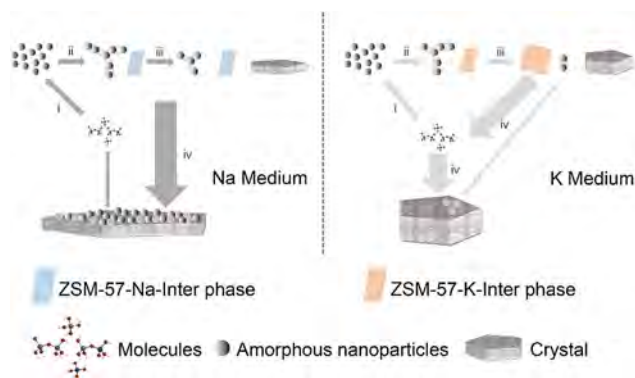


Figure 5. TEM images of the precursor after 54 h heating in the Na⁺ medium. a) Low-magnification morphology of the amorphous WLP precursor and initial ZSM-57-Na pentagonal nanoplate. b) HRTEM image of the corner structure of a ZSM-57-Na pentagonal nanoplate. The straight white line shows the twin boundary. The insert is an averaged image with *cm* symmetry imposed and the structural model of the MFS framework overlaid. c,d) SAED patterns of the highlighted areas of the ZSM-57-Na pentagonal nanoplate shown in Figure 5a.

ZSM-57-Na nanoplates and transform to crystalline ZSM-57-Na, which exists as larger pentagonal nanoflakes (ca. 1 μm) with a coarse surface (Figure 4a, 90–144 h). It should be noted that the larger nanoflakes are composed of numerous NASDs (20–50 nm), the sizes of which are comparable to those of the WLPs.

Based on the aforementioned investigations, a possible pathway for the crystallization of ZSM-57-Na is proposed as follows (Scheme 1, Na medium): i) Aggregated amorphous precursors (ca. 20 nm) emerge in a sol–gel of ZSM-57-Na; ii) the aggregated amorphous precursors cross-link to form a large quantity of WLPs; iii) the initial pentagonal ZSM-57-Na nanoplates and ZSM-57-Na-Inter with a smooth surface (ca. 400 nm) appear; iv) WLPs frequently attach to the initial pentagonal ZSM-57-Na nanoplates and transform in situ into a coarse multilayer surface with numerous crystallite fluctuations. The ZSM-



Scheme 1. Two different crystallization pathways to ZSM-57 zeolites: Non-classical (Na medium) and classical (K medium).

57-Na-Inter and WLPs are completely consumed in the final stage. In a short summary, the ZSM-57-Na zeolite crystallized in a Na⁺ medium undergoes classical solution-mediated (in the initial stage) and subsequent nonclassical solid-mediated pathways.

Crystallization mechanism of ZSM-57-K

For the ZSM-57-K sample, it is unambiguous that the pathway to its formation is different from that of the Na⁺-mediated system, as shown in Figure 4b and Scheme 1 (K medium). The initial stages (i, ii) of the crystallization mechanism are quite similar to those observed for ZSM-57-Na (Figure 4b, 24–72 h and Figure S6c,d in the Supporting Information), but with a different intermediate phase, ZSM-57-K-Inter (see Figure S9). Then in the next stage (iii), intact initial pentagonal nanoprisms with smooth surfaces (ca. 150 nm) start to emerge (Figure 4b, 96 h and Figure 6). At this stage, ZSM-57-K-Inter forms a major-

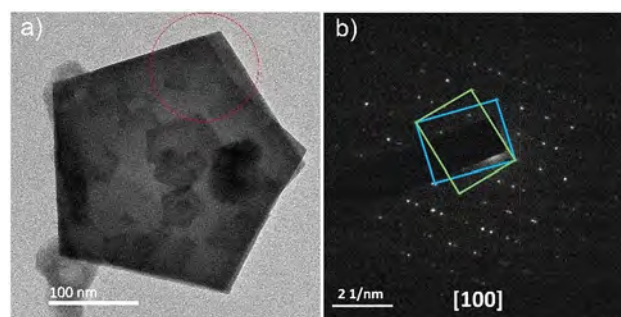


Figure 6. TEM images of the precursor after 96 h heating in the K⁺ medium. a) Typical morphology of a pentagonal ZSM-57-K nanoprism. b) SAED pattern of the encircled area in (a), and two ED datasets are shared by the *0kk* reflections.

ity and the WLPs a minority, which is different from the scenario observed in the ZSM-57-Na system (more WLPs and less intermediate phase). In the fourth stage (iv), the ZSM-57-K-Inter phase is also completely consumed, and the further growth of ZSM-57-K to large pentagonal prisms is attributed to the addition of silica molecules to the smooth surfaces of the initial pentagonal ZSM-57-K nanoprisms throughout the crystallization process, rather than to the attachment of amorphous WLPs (Figure 4b, 96–144 h). Generally, the crystallization procedure of ZSM-57-K zeolite is dominated by the classical liquid/solid process.

Although distinct crystal growth mechanisms occur in both systems, similar initial intact pentagonal ZSM-57 nanoplates/nanoprisms with smooth surfaces crystallize from the solution medium (liquid/solid, the classical pathway) after the induction period (as evidenced by the TEM results presented in Figures 5 and 6). This rare initial pathway for the crystallization process varies from the mechanisms previously reported for LTL-,^[42] CHA-,^[38] MTW-,^[41] and MFI-type^[52] zeolites, which involve the solid/solid-based nonclassical pathway of growth from amorphous nanoparticles. Thereafter, the distinct surface terrain fea-

tures ascribed to different crystallization pathways are also evidenced by AFM observations (see Figure S10 in the Supporting Information). Actually, the ZSM-57 zeolites obtained in the Na⁺ and K⁺ media also exhibit twin domains and tunability of the crystal domain size (see Figure S11). Compared with the frequent protrusions in the ZSM-57-Na sample attributed to the nonclassical crystal growth mechanism, the classical solution-mediated system derives a smooth layer surface structure in the ZSM-57-K sample, generating an intact pentagonal nanoprism with a few larger twin domains. It leaves a regular spiral contour on the final ZSM-57-K product (Figure 3a). Thus, the control of the crystallization mechanisms of the ZSM-57 zeolite can be realized by employing different alkali cations. Meanwhile, the size of twin domains in such zeolites can be tailored as well.

Furthermore, the pH value of the initial gel of the two different systems was considered (see Figure S12 in the Supporting Information). The initial pH value of the Na⁺ medium (13.1) is slightly lower than that of the K⁺ medium (13.3). When the pH values of the Na⁺ and K⁺ media are regulated to 13.3 and 13.1, respectively, ZSM-57 products mixed with impurities such as the MOR-type zeolite or quartz are obtained. Nevertheless, the morphologies of the obtained products remain nanoparticles (which are comparable to NASDs that do not aggregate into the larger pentagonal zeolite nanoflake) and intact pentagonal prisms in the Na⁺ and K⁺ media, respectively. Therefore, the crystallization pathways of the two systems are not affected by the pH value.

Catalytic performance evaluation

The unique running direction of the 10-ring pore openings (perpendicular to the ZSM-57-Na nanoflakes and ZSM-57-K nanoprisms) makes them promising catalysts for methanol conversion. The methanol conversion reaction was investigated with ZSM-57-Na and ZSM-57-K as catalysts under the same conditions (fixed bed, reaction temperature: 823 K, WHSV (weight hourly space velocity): 4 h⁻¹). Because the two catalysts have similar Si/Al ratios (ca. 21, see Table S1 in the Supporting Information) as well as surface areas and pore volumes (ZSM-57-Na: 345 m²g⁻¹, 0.15 cm³g⁻¹ vs. ZSM-57-K: 308 m²g⁻¹, 0.13 cm³g⁻¹, Table S2), their catalytic performances can be compared. As shown in Figure S13, the ZSM-57-Na nanoflake composed of NASDs displays a prolonged catalytic lifespan and a higher selectivity of lower olefins compared with the intact ZSM-57-K nanoprisms. The enhanced catalytic performance of ZSM-57-Na can be attributed to the short diffusion path in the thin zeolite nanoflakes, which facilitates the diffusion and provides more accessible active sites for the reactant molecules.

Conclusions

Electron crystallography combined with other techniques was utilized to unravel tunable twin domains in the medium-pore ZSM-57 zeolite. Because the twin domains share the *a* axis, the 10-ring pore openings run perpendicularly through the pen-

tagonal nanoflake of ZSM-57-Na and pentagonal nanoprism of ZSM-57-K. The tunable twin domain is ascribed to their distinct crystallization mechanisms. The classical solution-mediated pathway in the initial stage and the subsequent nonclassical solid-mediated pathway were identified in the Na⁺ medium. In the K⁺ medium, the classical solution-mediated pathway dominates the whole crystallization process. To our best knowledge, this is the first case of different types of alkali metal cations having been employed to tailor the distinct crystallization pathways of a specific zeolite.

Experimental Section

Preparation of ZSM-57 zeolite

Calculated amounts of Al(NO₃)₃·9H₂O (Sinopharm Chemical Reagent) and the OSDA were introduced into the required amount of deionized water to form a clear solution. Then, sodium hydroxide (Sinopharm Chemical Reagent) and silica gel (30% wt.) were added under vigorous stirring. After stirring for 12 h, a homogeneous gel with a general molar ratio of 60SiO₂/Al₂O₃/30NaOH (or 30KOH)/6OSDA/2400H₂O was acquired. Then the resultant gel was poured into a 35 mL Teflon-lined autoclave and crystallized at 433 K in the tumbling oven for different intervals of time. The final product was obtained by centrifugation and washed with deionized water to a neutral pH. Finally, the white paste was dried at 373 K in air overnight. Prior to the necessary measurements, the as-prepared sample was calcined at 873 K in air for 6 h to get rid of organic species. The proton form of the ZSM-57 zeolite was obtained by successive ion exchange with 1 M NH₄NO₃ at 353 K (three times) and finally calcined at 873 K for 3 h.

Materials characterization

PXRD patterns were recorded on a PANalytical diffractometer with Cu_{Kα} radiation ($\lambda = 1.5418 \text{ \AA}$) in reflection mode. Profile fittings of the PXRD patterns were performed with the TOPAS V5.0 Academic suite.^[55] Field emission scanning electron microscopy (FESEM) experiments were conducted on an Hitachi SU8020 instrument with an accelerating voltage of 2 kV at a working distance of 6 mm. To obtain the true morphologies, the zeolite samples were analyzed without coating conducting medium. Elemental analysis of the alkali metal cations, silicon, aluminium, and oxygen of the zeolite samples were collected by X-ray fluorescence (XRF) spectroscopy (Philips Magix-601). Thermogravimetric analyses (TGAs) were carried on a TA Q-600 instrument at a heating rate of 10 °Cmin⁻¹ in the temperature range 50–900 °C under an air flow of 100 mLmin⁻¹; the weight losses caused by the loss of water and the decomposition of the OSDAs were further confirmed by the corresponding differential analysis (DTA) curve. The surface features and height profiles were analyzed on a Bruker atomic force microscope (AFM, Bruker Dimensions ICO AFM) in ScanAsyst imaging mode. Solid-state MAS NMR spectra were recorded on a Bruker Avance III 600 spectrometer at a field of 14.1 T using a 4 mm WVT probe. The resonance frequencies for ²⁹Si, ¹³C, ²⁷Al, and ¹H NMR were 119.2, 150.9, 156.4, and 600.13 MHz, respectively. ¹H–¹³C CP MAS NMR spectra were recorded with a contact time of 4 ms and a recycle delay of 2 s at the spinning rate of 12 kHz; 400 scans were accumulated to obtain data of good signal-to-noise ratio. The chemical shifts were referenced to adamantane with the upfield methane peak at 29.5 ppm. ²⁷Al MAS NMR experiments were performed with a spinning rate of 12 kHz using one pulse sequence;

600 scans were accumulated with a 2 s recycle delay and a $\pi/8$ pulse width of 0.75 μs . Chemical shifts were referenced to $(\text{NH}_4)\text{Al}(\text{SO}_4)_2 \cdot 12\text{H}_2\text{O}$ at -0.4 ppm. ^{29}Si MAS NMR spectra were recorded with a spinning rate of 8 kHz using high-power proton decoupling; 1000 scans were accumulated with a 10 s recycle delay. Chemical shifts were referenced to 4,4-dimethyl-4-silapentanesulfonate sodium salt (DSS) at 0 ppm. N_2 sorption measurements (77 K) were carried out on a Micrometrics ASAP 2020 analyzer. Before the tests, the calcined ZSM-57 zeolite samples were degassed at 573 K for 4 h. The surface areas were evaluated by the BET method by choosing the adsorption branch. The pore volumes of the zeolite samples were calculated by the t -plot method.

The as-prepared ZSM-57 sample for RED data collection was dispersed in absolute ethanol and treated by ultrasonic treatment for 2 min, respectively. A droplet of the suspension was transferred onto a carbon-coated copper grid and dried in air. The collection of 3D RED data was controlled by the software RED data collection20 on a JEOL JEM2100 TEM at 200 kV. A single-tilt tomography sample holder was used for the data collection, which could tilt from -70 to $+70^\circ$ in the TEM. The HRTEM images were also acquired on the JEOL JEM2100 TEM at 200 kV.

Catalytic performance evaluation

ZSM-57-Na and ZSM-57-K were evaluated as catalysts in the methanol conversion reaction in a fixed bed quartz reactor. Each sample was preheated at 853 K for 1 h, and then the reaction temperature was lowered to 823 K. The feedstock was injected with the carrier gas N_2 at a flow rate of 40.0 mL min^{-1} . The consequential reaction was performed in an atmospheric pressure. The products were monitored by using an online Agilent 7890A GC equipped with a flame ionization detector.

Structure model building

The (011) crystallographic plane of the ZSM-57 zeolite was proposed as the twin boundary based on the structural investigations uncovered by electron crystallography. In addition, the twin structure model was built by using the Material Studios suite.^[56]

Acknowledgements

P.G. acknowledges financial support from the CAS Pioneer Hundred Talents Program (Y706071202). L.W. acknowledges the China Postdoctoral Science Foundation (2018M630308) and DICP Outstanding Postdoctoral Foundation (2017YB07).

Conflict of interest

The authors declare no conflict of interest.

Keywords: alkali metals · crystal growth · electron diffraction · transmission electron microscopy · twin structures · zeolites

- [1] <http://www.iza-structure.org/databases/>, Database of Zeolite Structures.
 [2] L. Wang, S. Zhu, M. Shen, H. Tian, S. Xie, H. Zhang, Y. Zhang, Y. Tang, *Angew. Chem. Int. Ed.* **2017**, *56*, 11764–11768; *Angew. Chem.* **2017**, *129*, 11926–11930.
 [3] M. Tong, D. Zhang, W. Fan, J. Xu, L. Zhu, W. Guo, W. Yan, J. Yu, S. Qiu, J. Wang, F. Deng, R. Xu, *Sci. Rep.* **2015**, *5*, 11521.

- [4] W. Chaikittisilp, Y. Suzuki, R. R. Mukti, T. Suzuki, K. Sugita, K. Itabashi, A. Shimojima, T. Okubo, *Angew. Chem. Int. Ed.* **2013**, *52*, 3355–3359; *Angew. Chem.* **2013**, *125*, 3439–3443.
 [5] L. Karwacki, M. H. F. Kox, D. A. M. de Winter, M. R. Drury, J. D. Meeldijk, E. Stavitski, W. Schmidt, M. Mertens, P. Cubillas, N. John, A. Chan, N. Kahn, S. R. Bare, M. Anderson, J. Kornatowski, B. M. Weckhuysen, *Nat. Mater.* **2009**, *8*, 959–965.
 [6] E. Stavitski, M. R. Drury, D. A. M. de Winter, M. H. F. Kox, B. M. Weckhuysen, *Angew. Chem. Int. Ed.* **2008**, *47*, 5637–5640; *Angew. Chem.* **2008**, *120*, 5719–5722.
 [7] J. B. Higgins, R. B. LaPierre, J. L. Schlenker, A. C. Rohrman, J. D. Wood, G. T. Kerr, W. J. Rohrbaugh, *Zeolites* **1988**, *8*, 446–452.
 [8] J. M. Newsam, M. M. J. Treacy, W. T. Koetsier, C. B. D. Gruyter, *Proc. R. Soc. London Ser. A* **1988**, *420*, 375–405.
 [9] T. Willhammar, J. Sun, W. Wan, P. Oleynikov, D. Zhang, X. Zou, M. Moliner, J. Gonzalez, C. Martínez, F. Rey, A. Corma, *Nat. Chem.* **2012**, *4*, 188–194.
 [10] J. L. Schlenker, W. J. Rohrbaugh, P. Chu, E. W. Valyocsik, G. T. Kokotailo, *Zeolites* **1985**, *5*, 355–358.
 [11] R. F. Lobo, H. van Koningsveld, *J. Am. Chem. Soc.* **2002**, *124*, 13222–13230.
 [12] S. Smeets, D. Xie, C. Baerlocher, L. B. McCusker, W. Wan, X. Zou, S. I. Zones, *Angew. Chem. Int. Ed.* **2014**, *53*, 10398–10402; *Angew. Chem.* **2014**, *126*, 10566–10570.
 [13] R. F. Lobo, M. Tsapatsis, C. C. Freyhardt, I. Chan, C.-Y. Chen, S. I. Zones, M. E. Davis, *J. Am. Chem. Soc.* **1997**, *119*, 3732–3744.
 [14] H. van Koningsveld, R. F. Lobo, *J. Phys. Chem. B* **2003**, *107*, 10983–10989.
 [15] Y. Zhao, Z. Ye, L. Wang, H. Zhang, F. Xue, S. Xie, X.-M. Cao, Y. Zhang, Y. Tang, *Cryst. Growth Des.* **2018**, *18*, 1101–1108.
 [16] X. Zhang, D. Liu, D. Xu, S. Asahina, K. A. Cychosz, K. V. Agrawal, Y. A. Wahedi, A. Bhan, S. A. Hashimi, O. Terasaki, M. Thommes, M. Tsapatsis, *Science* **2012**, *336*, 1684–1687.
 [17] D. Xu, G. R. Swindlehurst, H. Wu, D. H. Olson, X. Zhang, M. Tsapatsis, *Adv. Funct. Mater.* **2013**, *24*, 201–208.
 [18] M. Khaleel, A. J. Wagner, K. A. Mkhoyan, M. Tsapatsis, *Angew. Chem. Int. Ed.* **2014**, *53*, 9456–9461; *Angew. Chem.* **2014**, *126*, 9610–9615.
 [19] D. Zhang, P. Oleynikov, S. Hovmöller, X. Zou, *Z. Kristallogr.* **2010**, *225*, 94–102.
 [20] W. Wan, J. Sun, J. Su, S. Hovmöller, X. Zou, *J. Appl. Crystallogr.* **2013**, *46*, 1863–1873.
 [21] The Nobel Prize in Chemistry 1985, http://www.nobelprize.org/nobel_prizes/chemistry/laureates/1985/, (accessed July 10, 2017).
 [22] A. L. Patterson, *Phys. Rev.* **1934**, *46*, 372–376.
 [23] J. Christensen, P. Oleynikov, S. Hovmöller, X. D. Zou, *Ferroelectrics* **2004**, *305*, 273–277.
 [24] G. Oszlányi, A. Sütő, *Acta Crystallogr. Sect. A* **2008**, *64*, 123–134.
 [25] G. Oszlányi, A. Sütő, *Acta Crystallogr. Sect. A* **2004**, *60*, 134–141.
 [26] G. Oszlányi, A. Sütő, *Acta Crystallogr. Sect. A* **2005**, *61*, 147–152.
 [27] J. Wu, K. Leinenweber, J. C. H. Spence, M. O’Keeffe, *Nat. Mater.* **2006**, *5*, 647–652.
 [28] C. Baerlocher, L. B. McCusker, L. Palatinus, *Z. Kristallogr.* **2009**, *222*, 47–53.
 [29] C. Baerlocher, F. Gramm, L. Massüger, L. B. McCusker, Z. He, S. Hovmöller, X. Zou, *Science* **2007**, *315*, 1113–1116.
 [30] P. Guo, J. Shin, A. G. Greenaway, J. G. Min, J. Su, H. J. Choi, L. Liu, P. A. Cox, S. B. Hong, P. A. Wright, X. Zou, *Nature* **2015**, *524*, 74–78.
 [31] R. Martínez-Franco, M. Moliner, Y. Yun, J. Sun, W. Wan, X. Zou, A. Corma, *Proc. Natl. Acad. Sci. USA* **2013**, *110*, 3749–3754.
 [32] S. Smeets, L. B. McCusker, C. Baerlocher, D. Xie, C.-Y. Chen, S. I. Zones, *J. Am. Chem. Soc.* **2015**, *137*, 2015–2020.
 [33] S. Smeets, D. Xie, L. B. McCusker, C. Baerlocher, S. I. Zones, J. A. Thompson, H. S. Lacheen, H.-M. Huang, *Chem. Mater.* **2014**, *26*, 3909–3913.
 [34] P. Guo, K. Strohmaier, H. Vroman, M. Afeworki, P. I. Ravikovitch, C. S. Paur, J. Sun, A. Burton, X. Zou, *Inorg. Chem. Front.* **2016**, *3*, 1444–1448.
 [35] T. Willhammar, A. W. Burton, Y. Yun, J. Sun, M. Afeworki, K. G. Strohmaier, H. Vroman, X. Zou, *J. Am. Chem. Soc.* **2014**, *136*, 13570–13573.
 [36] W. Hua, H. Chen, Z.-B. Yu, X. Zou, J. Lin, J. Sun, *Angew. Chem. Int. Ed.* **2014**, *53*, 5868–5871; *Angew. Chem.* **2014**, *126*, 5978–5981.
 [37] A. I. Lupulescu, J. D. Rimer, *Science* **2014**, *344*, 729–732.

- [38] M. Kumar, H. Luo, Y. Román-Leshkov, J. D. Rimer, *J. Am. Chem. Soc.* **2015**, *137*, 13007–13017.
- [39] K. N. Olafson, R. Li, B. G. Alamani, J. D. Rimer, *Chem. Mater.* **2016**, *28*, 8453–8465.
- [40] H. Zhang, H. Zhang, Y. Zhao, Z. Shi, Y. Zhang, Y. Tang, *Chem. Mater.* **2017**, *29*, 9247–9255.
- [41] Y. Zhao, H. Zhang, P. Wang, F. Xue, Z. Ye, Y. Zhang, Y. Tang, *Chem. Mater.* **2017**, *29*, 3387–3396.
- [42] M. Kumar, R. Li, J. D. Rimer, *Chem. Mater.* **2016**, *28*, 1714–1727.
- [43] H. Greer, P. S. Wheatley, S. E. Ashbrook, R. E. Morris, W. Zhou, *J. Am. Chem. Soc.* **2009**, *131*, 17986–17992.
- [44] W. C. Paik, C.-H. Shin, J. M. Lee, B. J. Ahn, S. B. Hong, *J. Phys. Chem. B* **2001**, *105*, 9994–10000.
- [45] S.-H. Lee, C.-H. Shin, G. J. Choi, T.-J. Park, I.-S. Nam, B. Han, S. B. Hong, *Microporous Mesoporous Mater.* **2003**, *60*, 237–249.
- [46] J. L. Schlenker, J. B. Higgins, E. W. Valyocsik, *Zeolites* **1990**, *10*, 293–296.
- [47] S. Teketel, L. F. Lundegaard, W. Skistad, S. M. Chavan, U. Olsbye, K. P. Lil-lerud, P. Beato, S. Svelle, *J. Catal.* **2015**, *327*, 22–32.
- [48] Z. Wang, W. Wan, J. Sun, W. Carrillo-Cabrera, D. Grüner, X. Yin, S. Qiu, G. Zhu, X. Zou, *CrystEngComm* **2012**, *14*, 2204–2212.
- [49] J. Bae, J. Cho, J. H. Lee, S. M. Seo, S. B. Hong, *Angew. Chem. Int. Ed.* **2016**, *55*, 7369–7373; *Angew. Chem.* **2016**, *128*, 7495–7499.
- [50] M. B. Park, S. J. Cho, S. B. Hong, *J. Am. Chem. Soc.* **2011**, *133*, 1917–1934.
- [51] S. Gao, X. Wang, X. Wang, Y. Bai, *Microporous Mesoporous Mater.* **2013**, *174*, 108–116.
- [52] N. Ren, B. Subotić, J. Bronić, Y. Tang, M. D. Sikirić, T. Mišić, V. Svetličić, S. Bosnar, T. A. Jelić, *Chem. Mater.* **2012**, *24*, 1726–1737.
- [53] F. Di Renzo, F. Remoué, P. Massiani, F. Fajula, F. Figueras, T. Descourieres, *Zeolites* **1991**, *11*, 539–548.
- [54] P. Sharma, J. Yeo, M. H. Han, C. H. Cho, *J. Mater. Chem. A* **2013**, *1*, 2602–2612.
- [55] A. A. Coelho, TOPAS-ACADEMIC, v. 5.0, **2012**.
- [56] Accelrys Software Inc. Materials Studio, v. 6.0, **2012**.

Manuscript received: August 22, 2018

Revised manuscript received: October 10, 2018

Accepted manuscript online: October 10, 2018

Version of record online: December 12, 2018